Journal of Theoretical Biology 349 (2014) 1–11

Contents lists available at ScienceDirect

Journal of Theoretical Biology

journal homepage: www.elsevier.com/locate/yjtbi

Simulation of swimming of a flexible filament using the generalized lattice-spring lattice-Boltzmann method

Tai-Hsien Wu [a,b], Rurng-Sheng Guo [b], Guo-Wei He [c], Ying-Ming Liu [d], Dewei Qi [a,d,*]

[a] Department of Chemical and Paper Engineering, Western Michigan University, Kalamazoo, MI 49009, USA
[b] Department of Physics National Kaohsiung Normal University, Kaohsiung 82444, Taiwan
[c] Key Laboratory of Nonlinear Mechanics, Institute of Mechanics, Chinese Academy of Sciences, Beijing 100080, PR China
[d] Yangtze Center of Mathematics, Sichuan University, Chengdu 610064, PR China

HIGHLIGHTS

- We introduced a generalized lattice-spring lattice-Boltzmann model (GLLM) for numerical simulation of flexible bodies in fluids.
- Validation of GLLM is conducted by comparing our results with existing theoretical and experimental results.
- Swimming of a flexible filament driven by its header with a harmonic function is simulated at Reynolds numbers ranged 0.15–5.1.
- The wave patterns of the filament are consistent with the theory of elastohydrodynamics at low Reynolds number and the wave wriggles increase as the Reynolds number increases.
- Intensity of vortices and propulsive force increases as Reynolds number increases.

ARTICLE INFO

Article history:
Received 2 May 2013
Received in revised form
8 January 2014
Accepted 15 January 2014
Available online 28 January 2014

Keywords:
Lattice Boltzmann method
Lattice spring model
A flexible filament

ABSTRACT

A generalized lattice-spring lattice-Boltzmann model (GLLM) is introduced by adding a three-body force in the traditional lattice-spring model. This method is able to deal with bending deformation of flexible biological bodies in fluids. The interactions between elastic solids and fluid are treated with the immersed boundary-lattice Boltzmann method. GLLM is validated by comparing the present results with the existing theoretical and simulation results. As an application of GLLM, swimming of flagellum in fluid is simulated and propulsive force as a function of driven frequency and fluid structures at various Reynolds numbers 0.15–5.1 are presented in this paper.

© 2014 Elsevier Ltd. All rights reserved.

1. Introduction

In a fluid environment, self-propel locomotion is one of popular movements employed by various biological life, from small size with nanometer and submicron-meter, such as bacteria and microorganism, to large size with more than 10 m, for example, whale. The Reynolds number ranges from $Re = 10^{-5} \sim 10^{-1}$ for microorganism to $Re = 10^{7}$ for fish swimming. Taylor (1951) first explained how microorganisms could propel itself using the viscous force, then followed by Machin (1958) who calculated the locomotion patterns of flagellar-like swimmer. Wiggins et al. (1998) introduced a new theory called elastohydrodynamics. Later, the theory played a significant role in this field due to the ability of the prediction for the shape pattern and the propulsive force of flagellum. Lagomarsino et al. (2003) and Lowe (2003) used the slender body theory to simulate the flagellum locomotion. Their studies were summarized by Lauga and Powers (2009). In addition to the theory developments, many experimental works for micro-organism swimmers were also performed. For example, Wiggins and Goldstein (1998) measured the shape pattern and proposed bending moduli for the flagellum. Yu et al. (2006) measured the propulsive force for the swimming flagellum, Pak et al. (2011) designed a flexible nanowire motor to give a high speed propulsion for the flagellum. All the above work are based on the Stokes equation where inertia is ignored and the Reynolds number is zero. It is noted that the Stokes equation is identical under time reversal. As a result, Purcell (1977) introduced the general "scallop theorem" and pointed out that there is no net propulsive force under "reciprocal motion". However, as Reynolds number gradually and continuously increases to a non-zero value, the inertia may start to play a role due to the symmetry breaking down, and a

* Corresponding author at: Department of Chemical and Paper Engineering, Western Michigan University, Kalamazoo, MI 49009, USA.
E-mail address: dewei.qi@wmich.edu (D. Qi).

0022-5193/$ - see front matter © 2014 Elsevier Ltd. All rights reserved.
http://dx.doi.org/10.1016/j.jtbi.2014.01.021

net propulsive force may be produced, even in a very small Reynolds number. In particular, Lauga (2007) demonstrated that the breakdown of Purcell's scallop theorem with inertia can take place in a continuous way. In other words, as long as the Reynolds number is non-zero, the net force is non-zero. In fact, Leal (1980) pointed out that the inertial effects could be experimentally detected when the Reynolds number is as small as $Re=10^{-3}$. Therefore, in this paper we will focus on the motion of flagellum with a non-zero Reynolds number in the order of $Re=10^{-1}\sim 1$, corresponding to large ciliates, such as Paramecium (Lauga and Powers, 2009).

The elastohydrodynamics with the slender body theory, based on the Stokes laws, are extensively used for a very low Reynolds number case in this field. Simultaneously, a direct simulation method, which can deal with flexible and deformable body in a non-zero Reynolds number fluid, was developed. The first method, called immersed boundary method (IBM), was presented by Peskin (1977), Peskin (2002). In IBM, the Navier–Stokes equations are solved in a regular cubic lattice while the motion of an elastic body is described in a Lagrangian coordinate system. The force due to elastic body is computed by tracking the deformation of the flexible body and imposed on the nearby fluid grids. The fluid velocity is updated under the influence of the elastic force and the new velocity is then interpolated at the elastic body points, which are moved at the interpolated velocity. IBM is extensively used in blood flow, platelet aggregation during blood clotting, aquatic animal locomotion, etc. Later, a study of self-propelled anguilliform swimming was reported by Carling et al. (1998) who used a finite difference method to solve fluid dynamic equations. The deformation was described by a mass center coordinate and a shape coordinate. The two coordinates were linked by an angle or an orientation of the deformed structure. A similar method (Hu et al., 2007) has also been used to simulate forward breaking and backward locomotion of angulla. The method along with other methods was reviewed by Miller et al. (2013).

A lattice Boltzmann method was applied to the deformable body in fluids. Qi (2006) used the lattice Boltzmann method to attack the Navier–Stokes equation while a solid body was discretized as a chain of rigid segments contacting each other at the their ends through ball and socket joints that allow adjacent segments to be bent. Buxton et al. (2005) used the lattice Boltzmann method to solve the Navier–Stokes equations and a lattice spring method to model the deformation of a flexible body. The deformable solid body is discretized as individual particles located in a regular lattice and connected by a two-body spring force between two nearest neighboring solid particles as a bond. The two-body force can deal with extension and compression but cannot accurately handle the bending deformation, because the two-body central force is a function of distance between two neighboring solid particles and does not provide any bonding angle information between two adjacent bonds or springs. The angle information is necessary for accurate description of solid structures. For example, a triclinic structure has three unequal bonding angles. Without the bond angle data, one is not able to construct the triclinic solid lattice. In Buxton lattice-Boltzmann lattice-spring method (LLM), the interaction between the fluid and the solid particle was simply treated by a moving bounce-back boundary rule (Ladd, 1994), therefore, the hydrodynamic forces were not very smooth. To overcome this problem, the immersed boundary method originally proposed by Peskin (1977) was used to treat the interaction between fluid and a rigid solid body (not a flexible body) in the frame of the lattice Boltzmann equation by Feng and Michaelides (2004). Subsequently, based on the lattice Boltzmann approach, the immersed boundary method was used to deal with the coupling between the fluid flow and a flexible body by Wu and Aidun (2010) who used the same lattice-spring model as Buxton, which cannot deal with bending deformation due to the lack of three-body forces or angular bonds.

The purpose of the present work is to introduce a three-body force, through angular bonds among a central solid particle and its two nearest neighboring solid particles, into LLM and allow the model to handle the bending deformation of a flexible body, immersed in a fluid, in a Reynolds number range from zero to non-zero. This method is called a generalized lattice-spring lattice-Boltzmann method (GLLM). It is demonstrated in the next section that the three-body angular bond plays a critical role in GLLM. Without the three-body angular bond the deformable body would not be properly bent. In GLLM, the coupling of elastic solid body with fluids is treated by using the immersed-boundary method. The validation of GLLM is presented. Due to discrete characteristics of the solid body, the lattice spring model can also be used to construct any shape of flexible bodies, such as spherical, non-spherical and clinic structures and disk-shaped membrane. Potentially, motion and adhesion of leukocytes and cancer cells in blood fluid can be simulated effectively by using GLLM.

As an application, a flagellum, or a flexible filament is created by the generalized lattice-spring model (GLSM) and the flagellum is oscillated in fluid by driving its head to move following a pre-described harmonic function. The shape patterns of the flexible filament, propulsive force and fluid structures are computed and the results are compared with the theoretical and experimental results (Pak et al., 2011; Taylor, 1951). In simulation, various Reynolds numbers from $Re=0.15$ up to $Re=5.1$ are used.

The generalized lattice-spring lattice-Boltzmann method will be described in Section 2. The comparison of the present results with existing theory and simulation results will be presented in Section 3. The simulation of oscillation of a flexible flagellum will be conducted at various Reynolds numbers in Section 4. The conclusion is made in the last section.

2. Simulation method

2.1. Immersed-boundary lattice Boltzmann method

Immersed-boundary lattice Boltzmann method is a numerical method which combines the lattice Boltzmann method (LBM) with the immersed-boundary method.

In LBM, a group of lattice nodes are used to represent fluid. Each node has distribution functions f_σ and discrete velocity $\mathbf{e}_\sigma$, where σ depends on the chosen lattice model. The Boltzmann equation with Bhatanaga–Gross–Krook single relaxation time is

$$f_\sigma(\mathbf{r}+\mathbf{e}_\sigma,t+1)=f_\sigma(\mathbf{r},t)-\frac{1}{\tau}[f_\sigma(\mathbf{r},t)-f_\sigma^{eq}(\mathbf{r},t)] \tag{1}$$

where τ is the relaxation time and $f_\sigma^{eq}(\mathbf{r},t)$ is the equilibrium distribution function at position $\mathbf{r}$ and time t as

$$f_\sigma^{eq}=\omega_\sigma\rho_f\left\{1+3(\mathbf{e}_\sigma\cdot\mathbf{u})+\tfrac{9}{2}(\mathbf{e}_\sigma\cdot\mathbf{u})^2-\tfrac{3}{2}(\mathbf{u}\cdot\mathbf{u})\right\} \tag{2}$$

In this simulation, the D3Q15 lattice model is applied and the discrete velocity is given by

$$\mathbf{e}_\sigma=\begin{cases}(0,0,0), & \sigma=0\\ (\pm1,0,0),(0,\pm1,0),(0,0,\pm1), & \sigma=1\\ (\pm1,\pm1,\pm1), & \sigma=2\end{cases} \tag{3}$$

and the weight coefficient is

$$\omega_\sigma=\begin{cases}\frac{2}{9}, & \sigma=0\\ \frac{1}{9}, & \sigma=1\\ \frac{1}{72}, & \sigma=2\end{cases} \tag{4}$$

The fluid density ρ_f and the momentum density $\rho_f \mathbf{u}$ are given by

$$\rho_f = \sum_\sigma f_\sigma \tag{5}$$

$$\rho_f \mathbf{u} = \sum_\sigma f_\sigma \mathbf{e}_\sigma \tag{6}$$

The kinematic viscosity ν is related to the relaxation time τ and is given by

$$\nu = \tfrac{1}{3}(\tau - \tfrac{1}{2}) \tag{7}$$

The immersed-boundary method coupled with LBM was presented by Feng and Michaelides (2004). The fluid nodes are applied to a regular Eulerian grid, so every boundary solid node will not coincide with the exactly adjacent fluid node. Therefore, the fluid velocity at the boundary solid node can be extrapolated from the fluid velocity of the surrounding fluid nodes by using a discrete Dirac delta function (Peskin, 2002)

$$D(\mathbf{r}) = \begin{cases} \dfrac{1}{64h^3}\left(1+\cos\dfrac{\pi x}{2h}\right)\left(1+\cos\dfrac{\pi y}{2h}\right)\left(1+\cos\dfrac{\pi z}{2h}\right), & |\mathbf{r}| \le 2h \\ 0 & \text{otherwise} \end{cases} \tag{8}$$

where h is the lattice length. The fluid nodes are within a spherical volume Π of a radius of $2h$, centered at a given solid node. The fluid velocity $\mathbf{u}_f$ at the position of the solid boundary node is given by

$$\mathbf{u}_f(\mathbf{r}^b, t) = \int_\Pi \mathbf{u}(\mathbf{r}^l, t) D(\mathbf{r}^l - \mathbf{r}^b)\, d\mathbf{r}^l \tag{9}$$

where $\mathbf{r}^b$ is the boundary solid position and $\mathbf{r}^l$ is the position of the lattice fluid nodes within the sphere as shown in Fig. 1.

Only a part of particles on a plane is shown in this figure to illustrate the interaction between fluid and solid particles in a three-dimensional space. The small circles represent the fluid particles and the squares denote the solid particles. The squares with the thicker edges are the boundary solid particles which directly interact with their surrounding fluid particles within a sphere. For example, the velocities $\mathbf{u}(\mathbf{r}^l, t)$ of the fluid particles around the kth solid boundary particle (see Fig. 1a) are interpolated to the kth particle position in step 1 (see Fig. 1b) to have $\mathbf{u}_f(\mathbf{r}^b, t)$ using Eq. (9). Under the non-slip condition, the boundary solid node velocity is equal to the fluid node velocity, and thus the momentum difference represents the interaction force $\mathbf{F}^{int}$ on the solid boundary over one time step as follows:

$$\mathbf{F}^{int}(\mathbf{r}^b, t) = \rho_f(\mathbf{u}_f(\mathbf{r}^b, t) - \mathbf{u}_s(\mathbf{r}^b, t-1)) \tag{10}$$

Next, the discrete Dirac delta function is used again to distribute the reaction force to the surrounding fluid nodes

$$\mathbf{g}(\mathbf{r}^l, t) = -\int_\Gamma \mathbf{F}^{int}(\mathbf{r}^b, t) D(\mathbf{r}^l - \mathbf{r}^b)\, d\mathbf{r}^b \tag{11}$$

where $\mathbf{g}$ is the distributed reaction force and Γ is a spherical volume of a radius of $2h$, located at $\mathbf{r}^l$. The force distribution process is illustrated in step 2 of Fig. 1b. Finally, the reaction force term is added to the Boltzmann equation as follows:

$$f_\sigma(\mathbf{r}+\mathbf{e}_\sigma, t+1) = f_\sigma(\mathbf{r}, t) - \frac{1}{\tau}[f_\sigma(\mathbf{r}, t) - f_\sigma^{eq}(\mathbf{r}, t)] + 3\omega_\sigma(\mathbf{g}\cdot\mathbf{e}_\sigma) \tag{12}$$

2.2. Generalized lattice spring model

In a mesoscopic scale, the interparticle force can be regarded following Hooke's law. Based on this idea, Buxton et al. (2005) provided the lattice spring model to represent the elastic structure. The model consists of two parts: (1) a solid body is discretized into particles and the solid particles space regularly

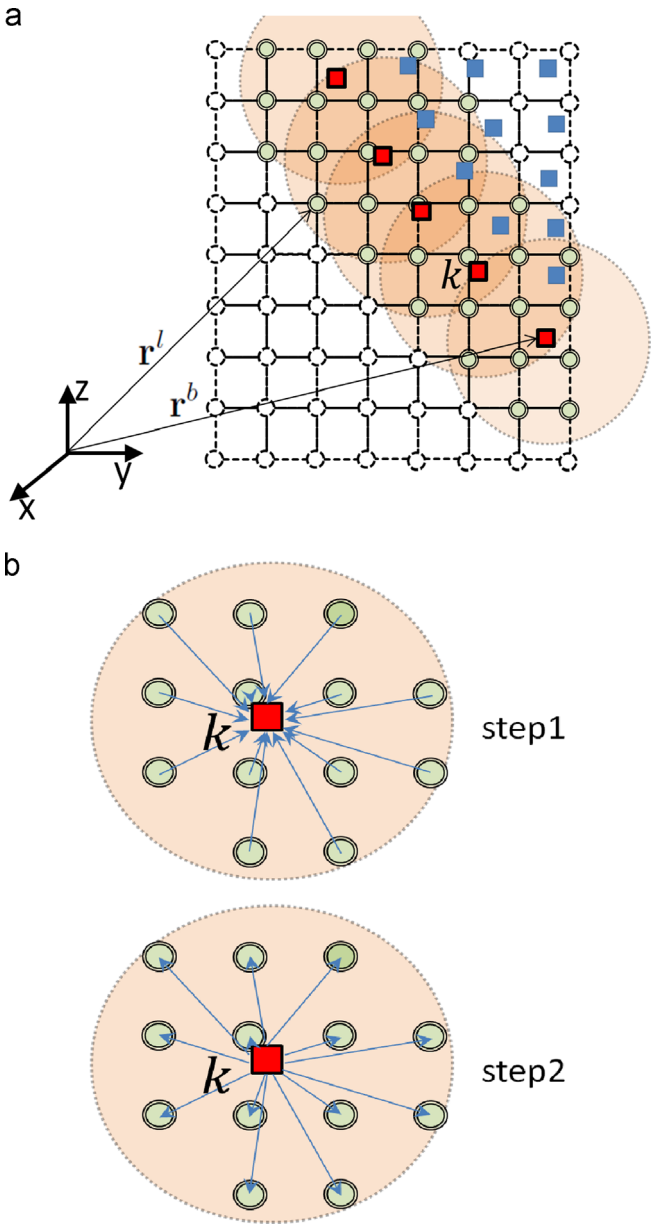

Fig. 1. (a) The small circles represent the fluid particles; the squares denote the solid particles; the large circles represent spheres around their central solid particle. (b) Step 1 shows that the flow velocities of fluid particles are interpolated to their central the kth solid particle and step 2 shows that the reaction force of the kth boundary solid particle on the fluid is interpolated to its surrounding fluid particles. The arrows denote the interpolation from the fluid to the solid particle positions in step 1 and from the solid to the fluid particle positions in step 2.

and (2) two adjacent particles are linked by a harmonic spring. In this way, the spring energy U^s acted on the ith node is given by

$$U_i^s = \frac{1}{2} k_s \sum_j (\mathbf{r}_{ij} - \mathbf{r}_{0ij})^2 \tag{13}$$

where k_s is the spring coefficient; $\mathbf{r}_{0ij}$ is the equilibrium length of the spring between two neighboring particles i and j; j are the nearest neighboring solid particle of the ith solid particle; $\mathbf{r}_{ij} = \mathbf{r}_i - \mathbf{r}_j$. The spring force is a two-body central force which allows either extension or compression between two solid particles and cannot handle bending deformation accurately as mentioned before. Therefore, it is necessary to include an additional three-body force among three solid particles to realize the bending

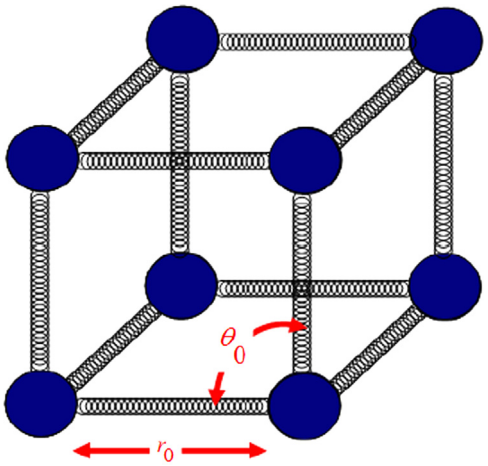

Fig. 2. The solid particles are located in a cubic lattice and the particle lattices are linked by springs and angular bonds.

deformation, called the generalized lattice-spring model (GLMS). Angular bonds are added and shown in Fig. 2.

The angular energy U^a is given by

$$U_i^a = \frac{1}{2}k_a \sum_j \sum_{k,k\neq j} (\theta_{ijk} - \theta_{0ijk})^2 \tag{14}$$

where k_a is the angular coefficient; j,k are the nearest neighboring solid particles of ith solid particle; θ_{ijk} is the angle between the bonding vector $\mathbf{r}_{ij}$ and the bonding vector $\mathbf{r}_{ik}$; θ_{0ijk} is the corresponding equilibrium angle. The elastic force F_i on the ith solid particle can be computed from the gradient of the total energy:

$$\mathbf{F}_i = -\nabla(U_i^s + U_i^a) \tag{15}$$

If the solid structure is isotropic, the elastic modulus of the solid body can be related to the spring and angular coefficients by

$$E = \frac{k_s}{r_0} \tag{16}$$

$$G \approx \frac{4k_a}{r_0^2} \tag{17}$$

where E is Young's modulus of the deformable solid body and G is its shear modulus. The derivation of the relationship between k_s and E and the relationship between k_a and G are presented in Appendix A.

The total force $\mathbf{F}_T^i = \mathbf{F}_i + \mathbf{F}^{int}$ drives the solid particle to move. The leap frog algorithm has been used to update the position and velocity of each solid particle at each time step by using the Newtonian mechanism. For details about the leap frog algorithm refer to Chapter 3 of the book by Allen and Tildesley (1987).

3. Validation

In all the simulations throughout this work, nondimensional units are used. One unit of time is 1.3×10^{-4} s and one unit of the length is 0.081 cm.

3.1. Beam model

To validate the generalized lattice-spring model (GLSM) of a rectangular cantilever beam a static force **F** acting at the right end of the beam is simulated using the generalized lattice-spring model while the left end of the beam is fixed as shown in Fig. 3. Four different sizes of the cantilever beams are used. The notation of (w, h, l) in Fig. 4 represents, respectively, the (width, height,

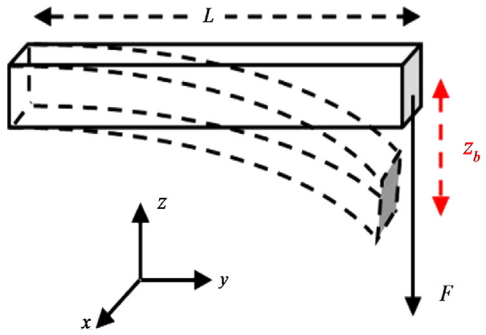

Fig. 3. A three-dimensional rectangular cantilever beam under a static force **F** at the beam right end. The left end is fixed. The deflection in the z-direction is z_b.

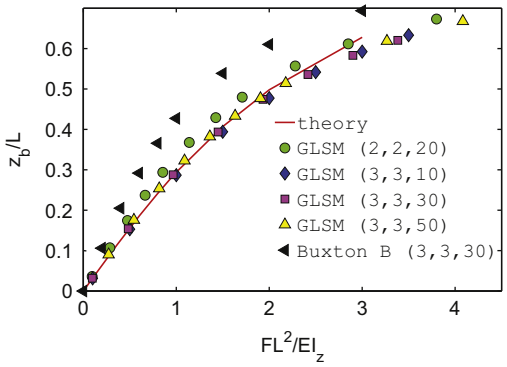

Fig. 4. The nondimensional normalized deflection as a function of the nondimensional normalized force for four different sizes of the cantilever beams. The red solid line is theoretical calculation results; the symbols are the simulation results for various beams. The results calculated by using Buxton model B is also shown. (For interpretation of the references to color in this figure caption, the reader is referred to the web version of this paper.)

length) of the beam in the non-dimensional length units (1 unit = 0.081 cm).

From the Euler–Bernoulli beam theory, the deflection is

$$z_b = \frac{FL^3}{3EI} \tag{18}$$

where L is the length of cantilever beam and EI is the bending rigidity. Eq. (18) is applied to the small deflection case, whereas the large deflection results have also been solved using the elliptic integration by Gere and Timoshenko (1987). It is noted that in the first order approximation it is assumed that shear modulus G is infinitely large in the Euler–Bernoulli beam theory and the shear deformation is ignored. In a higher order approximation, Timoshenko theory (Gere and Timoshenko, 1987) includes the shear deformation with a finite G and the deflection is

$$z_b = \frac{FL^3}{3EI}\left[1 + \frac{3EI}{\kappa GAL^2}\right] \tag{19}$$

where κ is the shear coefficient depending on geometry; $\kappa = \frac{5}{6}$ for the rectangular beam; A is the cross-sectional area. However, the deflection results of Timoshenko theory is not essentially different from those of Euler–Bernoulli for a long beam (with an aspect ratio about 10). The current study is limited to the long beam cases.

The simulation results of the non-dimensional normalized deflections as a function of the non-dimensional normalized force for four different sizes of the cantilever beams are displayed and compared in Fig. 4. The red line is the theoretical values; the symbols are the present simulation results for the beams with various sizes. The simulation results agree well with the theoretical results. As a comparison, the results of the deflection calculated by using Buxton model B, where each solid particle is

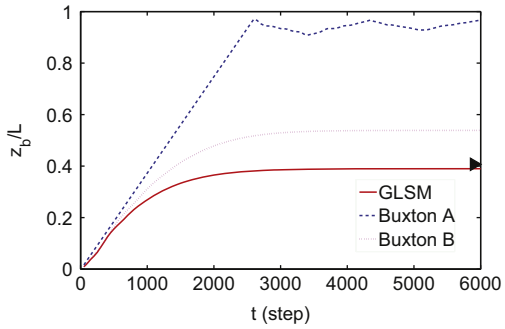

Fig. 5. The deflections as a function of time are compared among GLSM, Buxton model A and B. The triangle in the right axis denotes a theoretical deflection value. The beam size is (3,3,30).

bonded by its nearest and next nearest neighbors, are shown in the same figure for the beam of $(3, 3, 30)$. The error is very large as compared with the theoretical results. In addition, the results of the deflection against time are shown in Fig. 5 and compared among GLSM, Buxton model A and B. In Buxton model A, each solid particle is bonded by its nearest neighbors only. It is shown that the value of the deflection quickly approaches to the beam length for Buxton model A. In other words, Buxton model A cannot stand the bending deformation. While the deflection has a significant error for Buxton model B, the deflection results calculated by using GLSM are close to the theoretical value as shown by the triangle sign in Fig. 5.

3.2. Sedimentation of a flexible fiber

To further validate the GLLM, the sedimentation of a flexible fiber in fluid by the gravity is simulated by using two different methods: one is the present method and the other is the lattice Boltzmann flexible particle method (LBFPM), which was developed, validated and applied to simulate the flexible fiber suspensions and flexible wings (Qi, 2006; Qi et al., 2010; Liu et al., 2011) The simulation is performed in a box of $(N_x, N_y, N_z) = (2L, 4L, 1.1L) = (100, 400, 100)$ where $L=90$ is the length of the fiber. The walls are set at both the ends of the z-direction and a periodic condition is imposed in the x- and y-directions. The gravity is in the y-direction in Fig. 7(a). The long body of the fiber is initially lying along the x-direction with an initial velocity being equal to zero. A cylindrical and a rectangular fiber are used. Their aspect ratios are 9. The results of the sedimenting velocity as a function of time are shown in Fig. 7(a) for the rectangular fiber and in Fig. 7(b) for the cylindrical fiber, where the red solid lines are the results by using GLLM and the green dashed lines are those by using LBFPM. The Reynolds number is defined by $Re = v_0 L/\nu$, where v_0 is the terminal velocity of a very stiff fiber and L is the fiber length. The results by using the two methods are consistent with each other, demonstrating that GLLM faithfully describes a correct physical picture. The bending shape at an instance during sedimenting is shown in Fig. 6(a) for the rectangular fiber and in Fig. 6(b) cylindrical fibers where the GLLM is used.

3.3. Ellipsoidal particle in a shearing fluid

To provide more evidence, the motion of an ellipsoidal particle in a shearing fluid flow is simulated by using the GLLM. A very large rigidity with $k_s=1.2$ and $k_a=0.12$ for the solid particle is used in the simulation and its deformation can be ignored. A simulation box size is $(N_x, N_y, N_z) = (64, 64, 64)$. The sizes of ellipsoidal particles $(a, b, c) = (3, 3, 9)$ and $(3, 3, 6)$ are used, where a, b, c are the lengths of the semi-principal axes of the ellipsoid. The density of the solid particle is equal to the fluid density. The rotation of the ellipsoidal particle is located in the center of the simulation box and driven by a shear fluid imposed between two driving lips. The top lip is located at $z = N_z$ and has a velocity in the x-direction and the bottom lip is located at $z=0$ and has an opposite velocity to the top lip. The shear rate $\dot{\gamma} = 1.56 \times 10^{-4}$ in the simulation. The periodic conditions are imposed in other directions. The angular velocity simulation results are compared with those of Jeffrey (1922) theory at zero Reynolds number. According to Jeffery theory, a rigid ellipsoid in a simple shear flow will has a rotation angle ϕ and angular velocity $\dot{\phi}$ as a function of time as follows:

$$\phi = \tan^{-1}\left(\frac{b}{c}\tan\frac{bc\dot{\gamma}t}{b^2+c^2}\right) \tag{20}$$

$$\dot{\phi} = \frac{\dot{\gamma}}{b^2+c^2}(b^2\cos^2\phi + c^2\sin^2\phi) \tag{21}$$

The simulation results of the normalized angular velocity as a function of the time are compared with those of the Jeffery theory in Fig. 8, where the ellipsoids with two different aspect ratios c/b are used. The Reynolds number, defined by $Re = \dot{\gamma}c/\nu$, is 0.17. We have had a good agreement.

4. Swimming of a filament

The locomotion of a filament in fluid is an interesting subject and is intensively studied experimentally and theoretically by many biologists (Machin, 1958; Wiggins et al., 1998; Wiggins and Goldstein, 1998; Lagomarsino et al., 2003; Lowe, 2003; Yu et al., 2006; Lauga and Powers, 2009). Now, the motion of one-arm filament in fluid is simulated in various Reynolds numbers by using GLLM.

4.1. Wave pattern

An elastic filament with an aspect ratio of 10 is constructed and its motion is simulated by using the GLLM. The simulation boxes of a coarse grid of $(N_x, N_y, N_z) = (12.8D, 8.32L, 8L) = (64, 416, 400)$ and a fine grid of $(90, 582, 560)$ are used, respectively, to treat the same problem where D and L are the diameter and the length of the cylindrical flagellum, respectively. A periodic condition is imposed in the x-, y-, z-directions. The filament with $L=50$ or $L=70$ is located in the center of the simulation box as shown in Fig. 9. The density of the filament is the same as the fluid density. Two coefficients are set as $k_s=0.26$ and $k_a=0.025$ to ensure that the filament is flexible.

A driven point is located at the center of the cross section of the left end of the filament. The motion of the driven point follows a pre-described harmonic function with a small transverse amplitude

$$z = z_0 \sin \omega t \tag{22}$$

where $z_0 = 0.05L$ is the amplitude; $\omega = 2\pi f$; f is the frequency. The maximum velocity of the driven point is $v_1 = z_0\omega$. The right end is allowed to move freely.

Based on the elastohydrodynamics, when the inertia can be ignored, i.e., the Reynolds number is very small, Wiggins et al. (1998) obtained a solution of wave pattern, which is given by

$$z = \tfrac{1}{2} z_0[e^{-\tilde{C}\eta}\cos(\tilde{S}\eta+\omega t) + e^{-\tilde{S}\eta}\cos(\tilde{C}\eta-\omega t)] \tag{23}$$

where $\tilde{C} = \cos(\pi/8)$; $\tilde{S} = \sin(\pi/8)$; $\eta = y/l_\omega$. A characteristic length l_ω is defined by

$$l_\omega \equiv \left(\frac{EI}{\omega\zeta_\perp}\right)^{1/4} \tag{24}$$

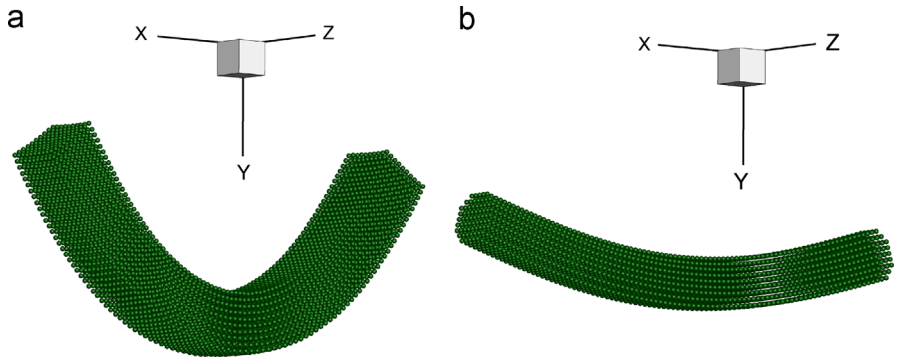

Fig. 6. The bending shape of the flexible fibers: (a) a rectangular solid and (b) cylinder.

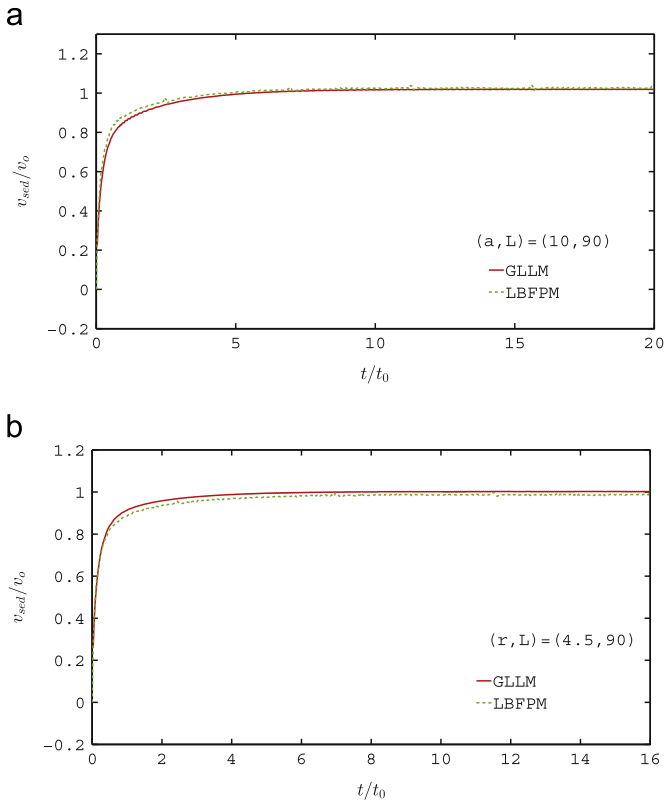

Fig. 7. The comparison of the GLLM results (red solid line) with the LBFPM results (green dashed line) (a) for the rectangular fiber and (b) for the cylindrical fiber. All sedimentation velocity v_{sed} is normalized by the terminal velocity v_0 and the time is normalized by $t_0 = L/v_0$. (a) The rectangular fiber of (a,L)=(10,90) where a is the width of the cross section and L is the length of the fiber.; Re=17.43; $\nu = 0.16$; EI=3902.17 with k_s=0.78 and k_a=0.075; the solid density $\rho_s = 1.2$; fluid density $\rho_f = 1.0$. (b) The cylindrical fiber of (r,L)=(4.5, L) where r is the radius of the cross section and L is the length of the fiber. Re=14.06, $\nu = 0.16$, EI=251.35 with k_s=0.78 and k_a=0.075; $\rho_s = 1.2$, $\rho_f = 1.0$. (For interpretation of the references to color in this figure caption, the reader is referred to the web version of this paper.)

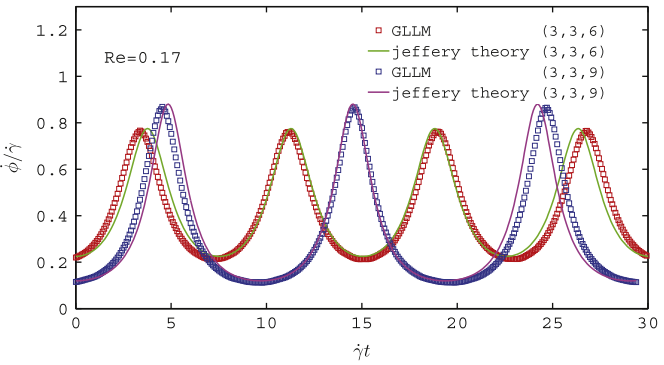

Fig. 8. The results of the normalized angular velocity as a function of the time are compared. The ellipsoids with the different aspect ratios of $c/b = 2$ and $c/b = 3$ are used. The solid lines are the Jeffery results and the square symbols are the simulation results. The Reynolds number is Re=0.17.

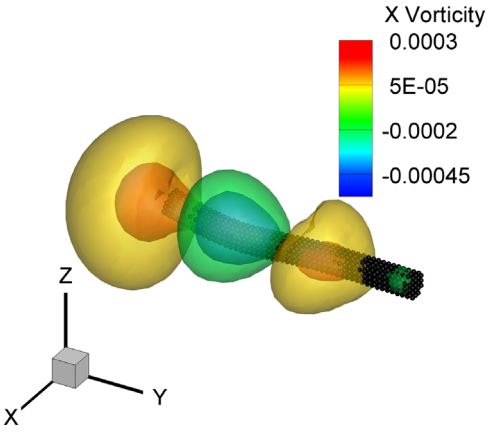

Fig. 9. The 3D fluid vorticity figure. The color iso-surfaces represent the vorticity on the x-direction and the black nodes represent the flagellum. (For interpretation of the references to color in this figure caption, the reader is referred to the web version of this paper.)

where the drag coefficient

$$\zeta_\perp = \frac{4\pi\mu}{\ln\left(\frac{L}{D}\right)+\frac{1}{2}}$$

is derived from the slender body theory, μ is the viscosity while the sperm number is defined by

$$Sp \equiv \frac{L}{l_\omega} \tag{25}$$

The simulation results of the wave patterns of the filament at different time instances are shown and compared with those of Wiggins et al. (1998) in Fig. 10, where the axes are normalized by the length of the filament. The lines labeled as "theory" are plotted from the analytic solution of Eq. (23) for the case of Sp=5. The simulation results agree well with the theory, indicating that the present developed method is reliable and can be used to simulate the locomotion of a flexible body.

Meanwhile, the wave patterns are compared between using the coarse grids and using the fine grids in Fig. 11. The agreement between the two wave patterns suggests that the coarse grids are good enough and will be used for this work.

One of the advantages of the direct simulation is that fluid structures can be extracted from fluid flow data while the same information cannot be obtained by using elastohydrodynamics

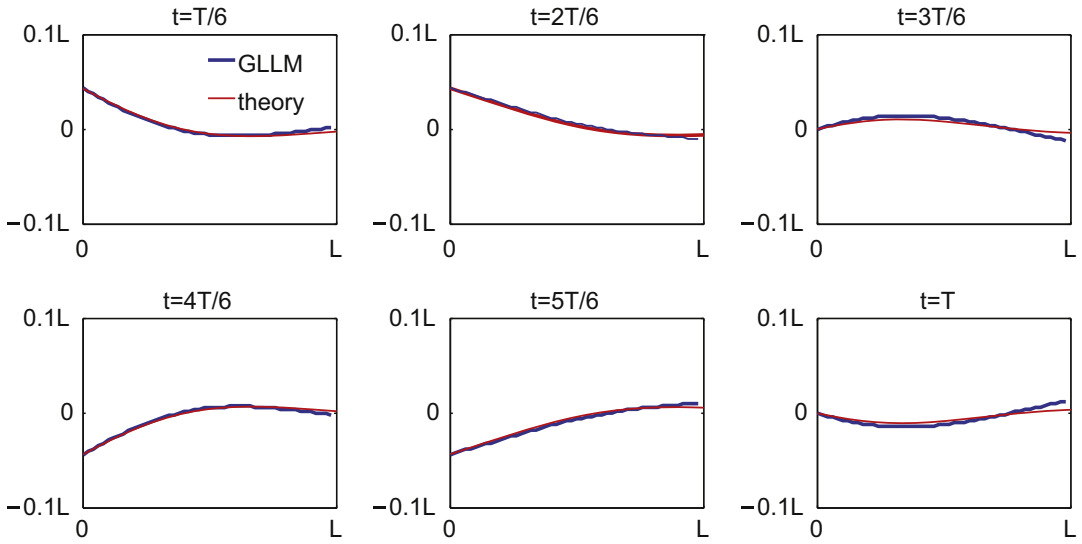

Fig. 10. The simulation results of the wave patterns of the filament at different time instances are compared with those of the theory results at $Sp=5$. The Reynolds number for the simulation is $Re=0.3$. The horizontal and the vertical axis are normalized by the length of filament L.

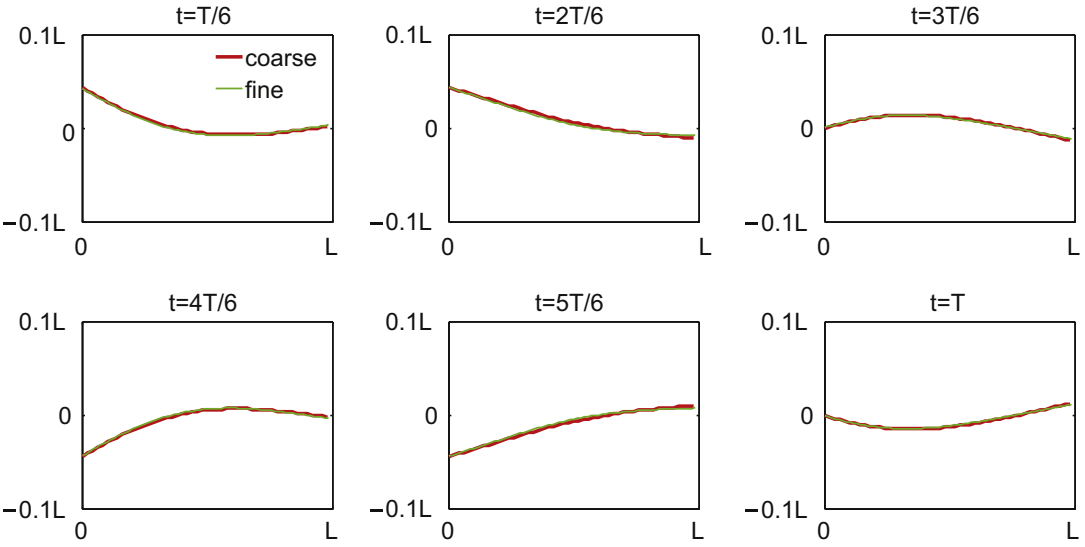

Fig. 11. The simulation results of the wave patterns of the filament at different time instances in the coarse grids are compared with those of the fine grids. the theory results at $Sp=5$. The Reynolds number for the simulation is $Re=0.3$. The horizontal and the vertical axis are normalized by the length of filament L.

and other analytic methods. The results of the contour of the vorticity in the x-direction along with the flow velocity vectors in the cross section of the yz-plane are computed and displayed in Fig. 12 for the case of $Re=0.3$ at $t=0.5T$ and $t=T$ where T is a period time.

As shown, during swimming, transverse movement may alter the local slope of the wave pattern and induce vortices even at very low Reynolds numbers. There are a pair of vortices with opposite sign, distributed and focused around the left driven end and the right free end, since the two ends experience a larger shearing force than the main body.

4.2. effects of inertia

In order to study the effect of inertia on the motion of filament, simulations are conducted at the same conditions except that Reynolds number ranges from $Re=0.15$ to $Re=5.1$. The wave patterns, fluid structures, propulsive force can be computed and compared at different Reynolds numbers. The propulsive force can be calculated by

$$F_y^h = \sum_i F_{iy}^h \tag{26}$$

where F_{iy}^h is the hydrodynamic force in the y-direction on the ith solid particle and the propulsive force coefficient is defined by

$$c^L = \frac{F_y^h}{0.5\rho_f DLv_1^2} \tag{27}$$

The average of any physics quantity, such as force, is a time average over the third through fifth cycles in this work.

The results of the average propulsive force as a function of driven frequency are shown in Fig. 13.

It shows that the average propulsive force is positively correlated to the frequency. As the frequency increases, the propulsive force increases.

The results of the average propulsive coefficient as a function of Reynolds number are shown in Fig. 14 where a double exponential fitting is attempted.

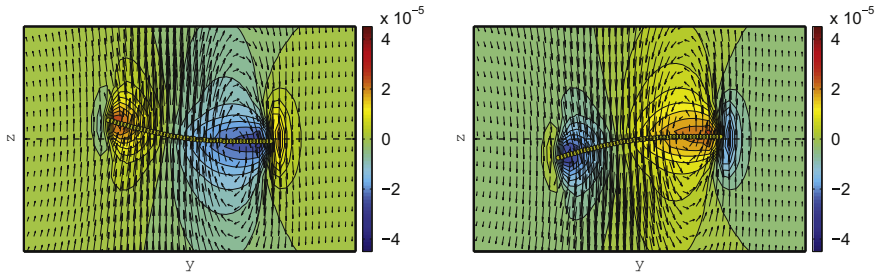

Fig. 12. The results of the vorticity in the x-direction along with the fluid velocity in the yz-plane at $t=0.5\,T$ (left) and $t=T$ (right) for the case of $Re=0.3$ are shown with the filament shape.

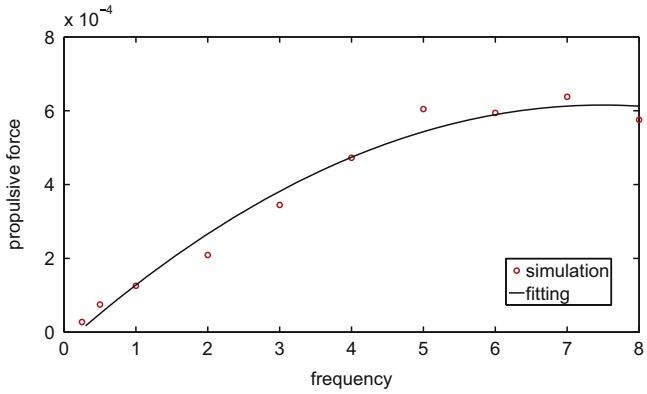

Fig. 13. The propulsive force as a function of the driven frequency. The red circles are simulation data and the black line is the fitting curve. (For interpretation of the references to color in this figure caption, the reader is referred to the web version of this paper.)

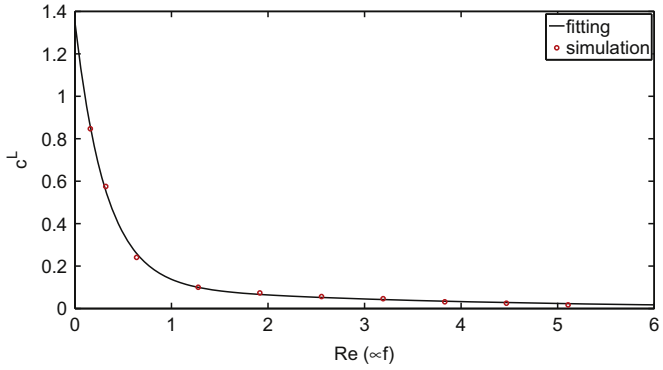

Fig. 14. The propulsive coefficient c^L as function of Reynolds number, The red circles are simulation data and the black line is the fitting curve. The fittings show that the propulsive coefficient decrease sharply at the low Reynolds number. (For interpretation of the references to color in this figure caption, the reader is referred to the web version of this paper.)

It shows that the average propulsive force coefficient c^L decreases with increasing the Reynolds number, dramatically for the Reynolds number $Re<1$, and then more slowly for $Re>1$.

The propulsive force as a function of time is compared among cases $Re=0.15$, 0.3 and 5.1 in Fig. 15. It shows that the propulsive force is much larger for $Re=5.1$ than for $Re=0.15$ and 0.3, illustrates that the propulsion increases as the Reynolds number increases due to inertia.

The wave patterns at different time instances within the fourth cycle are compared between cases $Re=0.3$ and $Re=5.1$ in Fig. 16.

At $t=T/6$ (T is the time period), there are two peaks on the curve of $Re=5.1$, one minimum and one maximum (if the two ends are not counted) while there is only one peak on the curve of $Re=0.3$. At $t=3T/6$ there are three peaks on the curve of $Re=5.1$

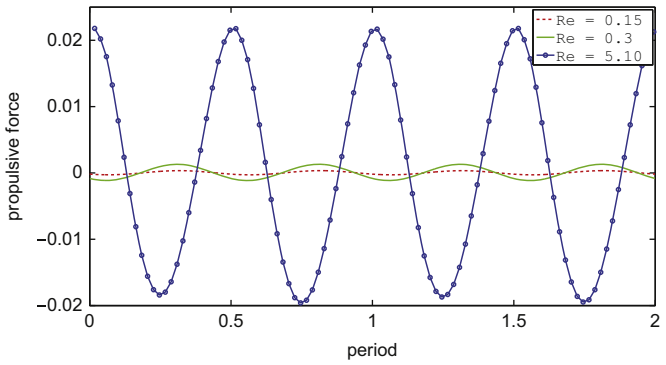

Fig. 15. The simulation results of the propulsive force f_P as a function of time are compared among cases $Re=0.15$, 0.3 and 5.1.

while there is only one peak on the curve of $Re=0.3$. Obviously, the case of $Re=5.1$ has richer waves than that of $Re=0.3$. The higher Reynolds number or the higher driven frequency results in more wriggles.

The results of the vorticity in the x-direction and the velocity in the yz-plane are compared between cases $Re=0.3$ and 5.1 in Fig. 17.

It shows that the intensity of the vorticity is much larger for $Re=5.1$ than for $Re=0.3$, indicating that the inertial effect greatly enhances propulsive forces as shown in Figs. 13 and 15. For a visualization purpose, a three-dimensional iso-surface of the vorticity is shown in Fig. 9 for the case of $Re=5.1$ at $t=T/2$.

When all the body of the filament is allowed to move freely in the horizontal or y-direction, the propulsive force will drive the filament to swim in the negative direction of the horizontal or y-axis. The results of the displacement $\Delta y/L=-(y(t)-y(0))$ and the velocity of the center of mass v_y in the y-direction as a function of time step are shown in Fig. 18.

It is shown that the swimming is much faster for the case of $Re=5.1$ than that of $Re=0.31$. In both the cases, the filament is migrating backward with clear oscillating in the y-direction.

5. Conclusion

In this paper, a GLLM is introduced by adding a three-body force into the lattice-spring model where only a two-body force is used. The current model allows one to simulate both bending and extension or compression deformation. It is demonstrated that the GLLM is reliable by comparing the present results with elastohydrodynamics and other existing results and is suitable for simulation of motion of flagellum. Subsequently, the GLLM is applied to simulate swimming of flagellum in a range of the Reynolds number 0.15–5.1. It is found that as the Reynolds number increases the propulsive force increases. A pair of vortices with opposite sign is distributed around the driven end and the free end. As the

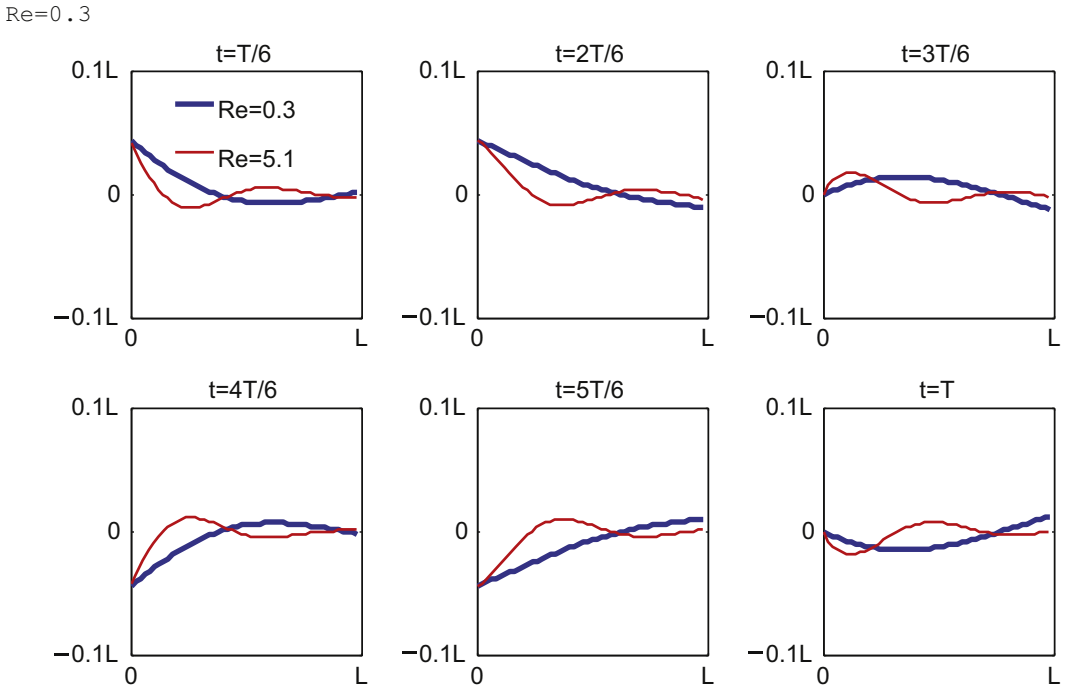

Fig. 16. The simulation results of the wave patterns of the filament at different time instances are compared between cases $Re=0.3$ and 5.1. The horizontal and vertical axis are normalized by the length of filament L.

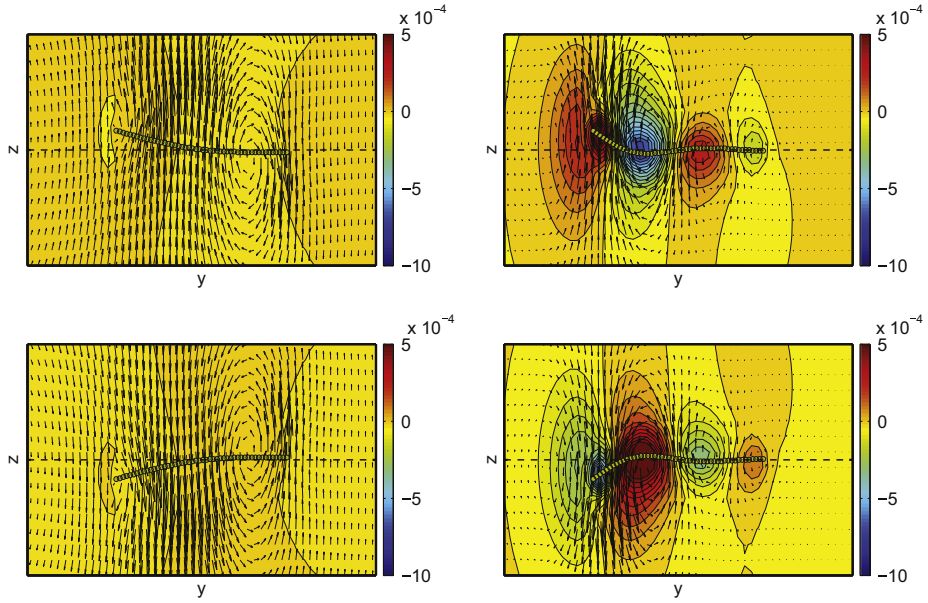

Fig. 17. The results of the vorticity in the x-direction and fluid velocity in the yz-plane at $t=0.5\,T$ (top) and $t=T$ (bottom) are compared between cases $Re=0.3$ (left) and 5.1 (right).

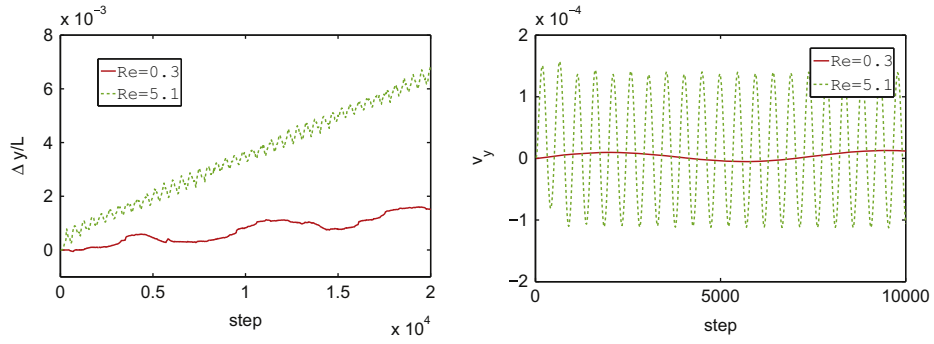

Fig. 18. The results of the freely swimming filament displacement(left) and velocity (right) in the y-direction are compared between the cases $Re=0.3$ and 5.1.

Reynolds number increases the intensity of the vorticity and the propulsive force increase due to inertial effects. It is also observed that the propulsive coefficient decreases with increasing the Reynolds number, dramatically for the Reynolds number $Re < 1$, and more slowly for the Reynolds number $Re > 1$.

Acknowledgments

We acknowledge the support from the National Science Foundation under Award Number 1126438 and the Funding Program for Encouraging University Students for Short-Term Overseas Study or Internship, sponsored by the Ministry of Education Taiwan. Qi also acknowledges the support from the Yangtze Center of Mathematics, Sichuan University when he visited the center and worked on this topic in the summer of 2011.

Appendix A. The relationship between the elastic modulus and coefficient

At the first part of this appendix, the relationship between Young's modulus E and spring coefficient k_s (Eq. (16)) is derived, and in the second part the derivation of relationship for the shear modulus and angular coefficient Eq. (17)) is shown.

A.1. Young's modulus and spring coefficient

In Fig. 19, the external tensile force $\mathbf{F}^{ext}$ only creates the tensile deformation Δr. On the equilibrium, the external force $\mathbf{F}^{ext}$ is equal to the interparticle elastic force $\mathbf{F}^e$, which includes the spring term and the angle term in GLLM. Because the deformation is only in the tensile direction, and the angular term is vanished

$$\mathbf{F}^{ext} + \mathbf{F}^e = \mathbf{F}^{ext} - \nabla(U^s + U^a) = \mathbf{F}^{ext} - \nabla U^s = 0$$

$$\mathbf{F}^e = \nabla U^s = k_s \Delta r$$

In Fig. 20, the area A_0 for a particle in GLLM is r_0^2.

According to Young's modulus definition, the tensile stress over tensile strain, the relationship can be shown as follows:

$$E = \frac{\text{tensile stress}}{\text{tensile strain}} = \frac{F^{ext}/A_0}{\Delta r/r_0} = \frac{k_s \Delta r/r_0^2}{\Delta r/r_0} = \frac{k_s}{r_0}$$

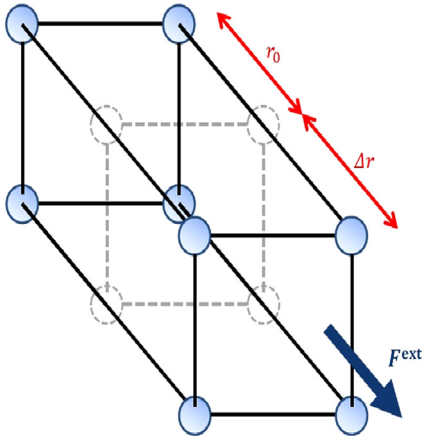

Fig. 19. The blue points are solid nodes and the black lines represent springs. Under the external force $\mathbf{F}^{ext}$, the spring, whose original length is r_0, would have the tensile deformation Δr. (For interpretation of the references to color in this figure caption, the reader is referred to the web version of this paper.)

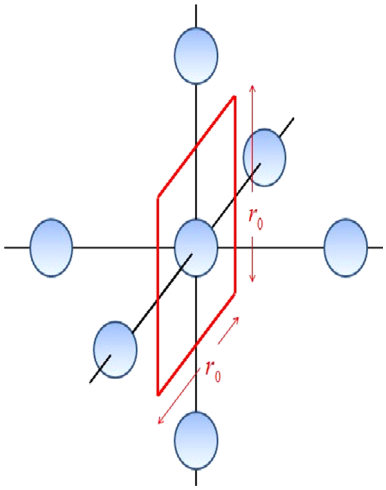

Fig. 20. The unit area of each node is a square (the red square) and its value is r_0^2. (For interpretation of the references to color in this figure caption, the reader is referred to the web version of this paper.)

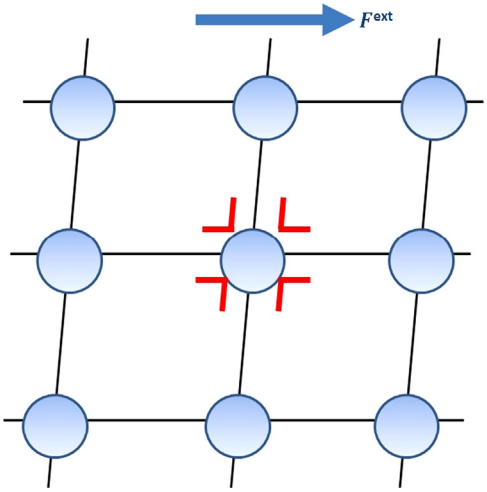

Fig. 21. For a particle, there are four angular elastic force $\mathbf{F}^e$ (the red marks) under the external force $\mathbf{F}^{ext}$. The spring has no deformation, and thus the interparticle angular elastic force F^e means angle bond force. (For interpretation of the references to color in this figure caption, the reader is referred to the web version of this paper.)

A.2. shear modulus and angular coefficient

For a given particle in the solid, there are four interparticle angular elastic forces $\mathbf{F}^e$ (the red marks in Fig. 21) under the external force $\mathbf{F}^{ext}$. For the shear deformation, the contribution from tensile spring term is zero and the shear modulus could be derived (see Figs. 21 and 22):

$$\mathbf{F}^{ext} + 4 \cdot \mathbf{F}^e = \mathbf{F}^{ext} - 4 \cdot \nabla(U^s + U^a) = \mathbf{F}^{ext} - 4 \cdot \nabla U^a = 0$$

$$\mathbf{F}^{ext} = 4k_a \Delta\theta$$

$$\frac{\Delta x}{r} = \tan\ \Delta\theta \approx \Delta\theta$$

$$G = \frac{\text{shear stress}}{\text{shear strain}} = \frac{4k_a \Delta\theta/r_0^2}{\Delta x/r} \approx \frac{4k_a}{r_0^2}$$

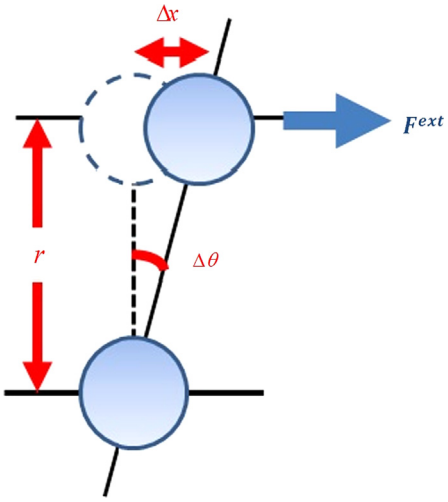

Fig. 22. Under the external force $\mathbf{F}^{ext}$, the angle distance $\Delta\theta$ is almost equal to $\Delta x/r$.

References

Allen, M.P., Tildesley, D.J., 1987. Computer Simulation of Liquids. Oxford University Press, New York.

Buxton, G.A., Verberg, R., Jasnow, D., Balazs, A.C., 2005. Newtonian fluid meets an elastic solid: coupling lattice Boltzmann and lattice-spring models. Phys. Rev. E 71, 056707.

Carling, J., Williams, T.L., Bowtell, G., 1998. Self-propelled anguilliform swimming: simultaneous solution of the two-dimensional Navier–Stokes equations and Newton's laws of motion. J. Exp. Biol. 201, 3143–3166.

Feng, Z.-G., Michaelides, E.E., 2004. The immersed boundary-lattice Boltzmann method for solving fluid–particle interaction problems. J. Comput. Phys. 195, 602–628.

Gere, J.M., Timoshenko, S.P., 1987. Mechanics of Materials, 2nd ed. Van Nostrand Reinhold Company, New York.

Hu, W., Tong, B., Liu, H., 2007. Dynamics of free straight swimming of angulla including forward, braking and backward locomotion. J. Hydrodyn., Ser. B 19, 395–402.

Jeffrey, G., 1922. The motion of ellipsoidal particles immersed in a viscous fluid. Proc. R. Lond., Ser. A 102, 161.

Ladd, A., 1994. Numerical simulations of particle suspensions via a discretised Boltzmann equation. Part 1: theoretical foundation. J. Fluid Mech. 271, 285.

Lagomarsino, M.C., Capuani, F., Lowe, C.P., 2003. A simulation study of the dynamics of a driven filament in an aristotelian fluid. J. Theor. Biol. 224, 215–224.

Lauga, E., 2007. Continuous breakdown of Purcell's scallop theorem with inertia. Phys. Fluids 19, 061703.

Lauga, E., Powers, T.R., 2009. The hydrodynamics of swimming microorganisms. Rep. Prog. Phys. 72, 096601.

Leal, L.G., 1980. Particle motions in a viscous fluid. Annu. Rev. Fluid Mech. 12, 435.

Liu, Y., Wu, T.-H., Guo, R.-S., Lee, Y.-H., Qi, D., 2011. Dynamics of sedimentation of flexible fibers in moderate Reynolds number flows. Comput. Fluids 48, 125–136.

Lowe, C.P., 2003. Dynamics of filaments: modelling the dynamics of driven microfilaments. Phil. Trans. R. Soc. Lond. B 358, 1543–1550.

Machin, K.E., 1958. Wave propagation along flagella. J. Exp. Biol. 35, 796–806.

Miller, L.A., Goldman, D.I., Hedrick, T.L., Tytell, E.D., Wang, Z.J., Yen, J., Albe, S., 2013. Using computational and mechanical models to study animal locomotion. Integr. Comp. Biol. 52, 553–575.

Pak, O.S., Gao, W., Wang, J., Lauga, E., 2011. High-speed propulsion of flexible nanowire motors: theory and experiments. Soft Matter 7, 8169–8181.

Peskin, C., 1977. Numerical analysis of blood flow in the heart. J. Comput. Phys. 25, 220–252.

Peskin, C.S., 2002. The immersed boundary method. Acta Numer., 479–517

Purcell, E.M., 1977. Lift at low Reynolds number. Am. J. Phys. 45, 3–11.

Qi, D., 2006. Direct simulations of flexible cylindrical fiber suspensions in finite Reynolds number flows. J. Chem. Phys. 125, 114901–114910.

Qi, D., Liu, Y., Shyy, W., Aono, H., 2010. Simulations of dynamics of plunge and pitch of a three-dimensional flexible wing in a low Reynolds number flow. Phys. fluids 22, 091901.

Taylor, G., 1951. Analysis of the swimming of microscopic organisms. Proc. R. Soc. Lond., Ser. A 209, 447–461.

Wiggins, C.H., Goldstein, R.E., 1998. Flexive and propulsive dynamics of elastica at low Reynolds number. Phys. Rev. Lett. 80, 3882–3979.

Wiggins, C.H., Riveline, D., Ott, A., Goldstein, R.E., 1998. Trapping and wiggling: elastohydrodynamics of driven microfilaments. Biophys. J. 74, 1043–1060.

Wu, J., Aidun, C.K., 2010. Simulating 3d deformable particle suspensions using lattice Boltzmann method with discrete external boundary force. Int. J. Numer. Meth. Fluids 62, 765–783.

Yu, T.S., Lauga, E., Hosoi, A.E., 2006. Experimental investigations of elastic tail propulsion at low Reynolds number. Phys. Fluids 18, 091701.